

# Performance limits on three-dimensional particle localization in photon-limited microscopy

Ginni Grover,\* Sri Rama Prasanna Pavani,<sup>†</sup> and Rafael Piestun

Department of Electrical, Computer and Energy Engineering, University of Colorado, Boulder, Colorado 80309, USA

\*Corresponding author: ginni.sharma@colorado.edu

Received February 17, 2010; revised July 28, 2010; accepted August 11, 2010;

posted September 9, 2010 (Doc. ID 124339); published September 30, 2010

We present the performance limits on three-dimensional (3D) localization accuracy of currently used methods of wide-field superlocalization microscopy. The three methods investigated are double-helix microscopy, astigmatic imaging, and biplane detection. In the shot-noise limit, Cramer–Rao lower bound calculations show that, among these techniques, the double-helix microscope exhibits the best axial and 3D localization accuracy over short as well as long depth-of-field systems. The fundamental advantage of engineered point-spread function systems, like the double-helix, stems from the additional degrees of freedom available to control diffraction in three dimensions over variable regions of interest. © 2010 Optical Society of America

OCIS codes: 110.3055, 180.6900, 110.4850.

Particle localization [1] is a critical task in multiple areas of science and engineering, including biophysics [2], nanofabrication [3], and superresolution microscopy [4,5]. To extend localization to three dimensions, conventional microscopes are typically modified, because they are suboptimal for axial localization [6–8]. Modified systems seek to (i) increase the sensitivity to axial position changes within the depth of field (DOF), (ii) increase the detected signal-to-noise ratio (SNR) of particles located out-of-focus, which are otherwise significantly blurred, and (iii) break the symmetry of the point-spread function (PSF) about the focal plane that results in axial position ambiguities for particles located on either side of the focal plane.

Accordingly, localization in the axial dimension has been demonstrated by defocusing conventional microscopes to operate outside the focal region [9], astigmatic imaging [10,11], simultaneous multiplane imaging [7,12], double-helix (DH) microscopy [8,13,14], and  $4\pi$  interferometric imaging [15,16]. Of these methods, the first four are appealing because of their simplicity and the ease with which they can be implemented in standard microscopes. While  $4\pi$  interferometric microscopy collects twice as many photons as the other techniques and improves accuracy via interference, it works on a short DOF and requires a complex setup (two objective lenses, precise interferometric paths, and multiple detectors). Comparisons of the biplane and the astigmatic methods have been reported in [15,17].

In this Letter, we present an information theoretical comparison of three-dimensional (3D) particle localization methods that use a single objective lens for wide-field photon-limited imaging, namely, defocus, astigmatic, biplane, and DH imaging. We use the Cramer–Rao bound (CRB) metric to determine the performance limit on accuracy achievable for position estimation. This study shows that, in the fundamental case of shot-noise limited detection, the DH microscope presents the lowest and most uniform 3D CRB over the entire range of interest, for short as well as long DOF systems.

In astigmatic imaging, a cylindrical lens is introduced in the imaging path to create an elongated response with orthogonal orientations on each side of the focal plane

[10,11]. Biplane detection [7] involves a modified microscope that simultaneously focuses on two planes within the sample, providing two images to estimate the axial position of a particle. A DH-PSF [8] is implemented by introducing a predesigned phase mask in the back focal plane of a microscope. The mask modifies the 3D response of the system to create two lobes that rotate around the axis with defocus, providing enhanced axial position information. Figure 1 shows, for these three techniques, transverse cross sections of the PSFs as they evolve through focus for a high-NA (1.4) imaging system with a 633 nm wavelength. Figure 1(a) shows the PSF for an astigmatic system, and Fig. 1(b) shows the PSFs side-by-side for the two imaging paths in the biplane method. The bottom two rows show different DH-PSF designs for operation over a  $2\ \mu\text{m}$  range [DH-PSF-1, Fig. 1(c)] and a shorter range [DH-PSF-2, Fig. 1(d)]. While astigmatic and biplane systems have only one parameter for optimization—astigmatism and relative defocus, respectively—engineered PSFs, such as the DH-PSF, present multiple degrees of freedom

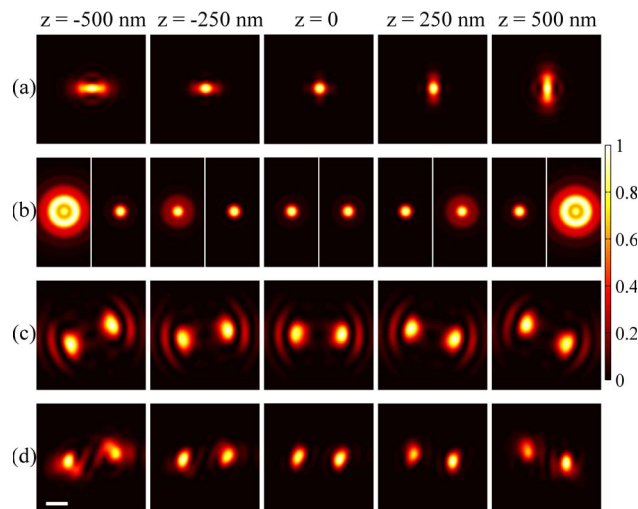


Fig. 1. (Color online) Transverse cross sections of the 3D PSFs shown for the (a) astigmatic PSF, (b) biplane system, (c) DH-PSF-1, and (d) DH-PSF-2. All images are normalized. See text for details. (Scale bar = 500 nm.)

to design the 3D PSF according to a specific estimation task [18,19].

The task of 3D particle localization is formalized as a statistical parameter estimation problem with parameter  $\mathbf{r} = (x, y, z)$ , the particle position [6–8]. For a given system (PSF), the CRB provides the best estimation performance using unbiased estimators. Explicitly,

$$\text{var}(\hat{\theta}) \geq \text{CRB}(\theta), \quad (1)$$

where  $\text{var}(\hat{\theta})$  is the variance of any unbiased estimator  $\hat{\theta}$  and  $\theta$  is the vector parameter to be estimated. For 3D position estimation, the 3D CRB, defined as  $\text{CRB}_{3D}(z) = [\text{CRB}_x(z) + \text{CRB}_y(z) + \text{CRB}_z(z)]/3$ , is a fundamental measure of the localization performance of the system. For shift variant systems the CRB is a function of  $(x, y, z)$ . The axial and overall performance over the region of interest,  $\Delta z$ , is evaluated as

$$\text{Avg} [\text{CRB}_z] = \frac{1}{\Delta z} \int_{\Delta z} \text{CRB}_z(z) dz, \quad (2)$$

$$\text{Avg} [\text{CRB}_{3D}] = \frac{1}{\Delta z} \int_{\Delta z} \text{CRB}_{3D}(z) dz, \quad (3)$$

respectively. Hence  $\text{Avg} [\text{CRB}_{3D}]$  is a single-parameter performance limit on the accuracy achievable in position estimation over a 3D domain.

The fundamental localization limit is obtained under the shot-noise limit with no other noise sources considered. In such cases, noise is modeled as a Poisson process [7,8]. The detector pixelation and external noise sources deteriorate the performance [7]. Here we compare the CRBs for shot-noise limited and pixelated detection (see [6,8] for the CRB calculation method).

A comparison of performance limits on localization, via  $\text{CRB}_{x,y,z}(z)$  and  $\text{CRB}_{3D}(z)$  for a single particle using the three methods discussed above and the standard PSF is presented in Figs. 2(a)–2(d). The common parameters for the calculation are  $\text{NA} = 1.4$ ,  $M = 100\times$ , detector pixel size =  $6.3 \mu\text{m} \times 6.3 \mu\text{m}$ , and area =  $79 \times 79$  pixels with a 100% fill factor. All calculations are based on a scalar wave model, as described in [6,8]. The emission/scattering from the particles is assumed to be monochromatic at 633 nm. Noise is modeled as a Poisson process with 10,000 photons crossing the pupil for all the systems. Because of the finite detector area, a slightly lower number of photons hit the detector as the different PSFs spread out.

In the biplane system, the detection planes are assumed to be 500 nm apart, in agreement with [7,15]. Increasing the image plane separation reduces the localization accuracy in  $x$  and  $y$ , while improving the accuracy in  $z$ , indicating that there is an optimum separation [15]. For comparison, the biplane CRB curve is shifted by +250 nm in Figs. 2(a)–2(d). In the astigmatic PSF calculation, the  $x$  and  $y$  foci are shifted by  $\pm 250$  nm by introducing a cylindrical lens [11]. Here, as in the biplane case, there is a trade-off between lateral and axial localization accuracy with respect to the two foci separation [15]. Two DH-PSF designs are analyzed to demonstrate the

flexibility in 3D PSF engineering: DH-1 was presented in [18], while DH-2 is a new design constrained to operate on a shorter DOF than DH-1 but still longer than the DOF of the studied astigmatic and biplane systems. The lower CRB of DH-2 relative to DH-1 is the result of higher light efficiency in the focal region and hence a better SNR over a shorter DOF [18,19].

Figures 2(a) and 2(b) show the CRBs for transverse localization. In the  $x$  direction, the DH-PSFs show the best performance in terms of accuracy and depth range, while in the  $y$  direction, the DH-PSFs perform worse for short depth range but still best for longer ranges. Nevertheless, the main advantage of DH-PSFs is in improving the  $\text{CRB}_z$  and overall 3D performance, as shown in Figs. 2(c) and 2(d). Figures 2(e) and 2(f) present the average axial and average 3D CRBs for depth ranges up to  $2 \mu\text{m}$ . These plots are aimed at establishing the best options for a given depth range. Accordingly, for each depth range value [abscissa in Figs. 2(e) and 2(f)] we found the depth region of each PSF that minimizes  $\text{CRB}_z$  [Fig. 2(c)] or  $\text{CRB}_{3D}$  [Fig. 2(d)]. Interestingly, the standard PSF performs exceptionally well for a short depth range of a few hundred nanometers [Fig. 2(f)]. As opposed to localization in two dimensions, in 3D the optimum localization is obtained by spreading of the PSF to a certain degree, affecting the density of particles that can be localized in parallel (Fig. 1). The DH-1 has the most uniform CRBs

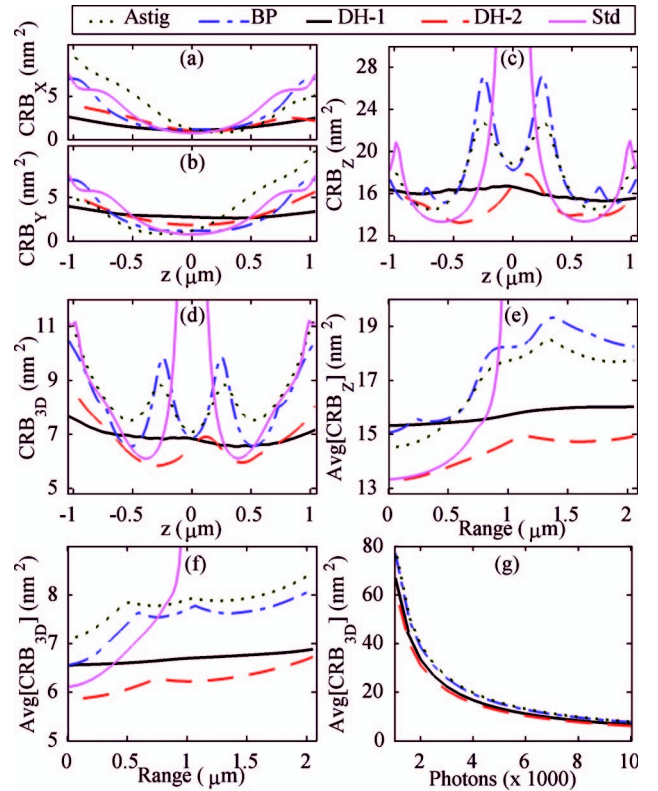


Fig. 2. Comparison of the CRBs for astigmatic PSF (Astig), biplane PSF (BP), DH-1, DH-2, and standard PSF (Std). (a)–(d) Show  $\text{CRB}_x(z)$ ,  $\text{CRB}_y(z)$ ,  $\text{CRB}_z(z)$ , and  $\text{CRB}_{3D}(z)$ , respectively, as a function of the  $z$  position. (e), (f) Show the variation in average  $\text{CRB}_z$  and  $\text{CRB}_{3D}$  with the depth range of measurement. (g) Shows the scaling of the average  $\text{CRB}_{3D}$  for  $1 \mu\text{m}$  range as a function of the number of detected photons. See text for details.

for a range of 2  $\mu\text{m}$ , while the DH-2, which is designed for a shorter range, has the lowest average  $\text{CRB}_z$  and  $\text{CRB}_{3D}$  for ranges up to 2  $\mu\text{m}$ . From 500 nm to 2  $\mu\text{m}$  DOF, the average  $\text{CRB}_{3D}$  for the DH-PSFs increases slowly. The biplane and astigmatic PSFs present at least 16% to 25% higher  $\text{CRB}_{3D}$  than DH-2 in this region. Similarly, the corresponding average  $\text{CRB}_z$  is at least 20% to 25% higher for the biplane and astigmatic PSFs. Therefore, the DH-PSFs present the lowest and most uniform accuracy over a longer DOF.

The parameters used in these CRB calculations are representative of typical experimental conditions [8,11,13,16]. When system parameters such as NA, wavelength, number of photons, and pixel size change, the relative behavior of the CRB remains essentially the same with the underlying assumptions of shot-noise limit and at least Nyquist sampling on the detector. In particular, the plots of Figs. 2(a)–2(d) scale with the number of photons  $N$ , as  $1/N$ , as shown in Fig. 2(g), for Avg [ $\text{CRB}_{3D}$ ] and a range of 1  $\mu\text{m}$ . Hence, these CRB results can be applied for comparison of a wide range of microscopy systems.

In this study, other noise sources such as background and readout noise are not considered. Nevertheless, there is a general trade-off between the DOF and the performance in the presence of background noise, which is the result of the widening of the PSF as the designed DOF is increased. Accordingly, DH-2 will be more resistant to background noise than DH-1. For instance, with 1000 detected photons and 1 photon/pixel background, along a range of 1  $\mu\text{m}$ , the Avg [ $\text{CRB}_{3D}$ ] in the astigmatic system will be lower than in the DH-1 but still higher than in the DH-2. This indicates that the 3D PSF can be optimized according to specific experimental conditions such as DOF and SNR. Also not considered here is the bandwidth of the emission or scattering, here assumed to be monochromatic, as in most other studies. In any case, for broader emission spectra, we have observed that the relative behavior of the performance limits is similar, with DH-2 having the lowest CRB. All these additional aspects will be discussed elsewhere.

In summary, we have shown a comparison of the performance limits, in shot-noise limited imaging, on the 3D particle localization accuracy for methods used in wide-field photon-limited microscopy. The results suggest that the 3D PSF can be engineered to achieve the best axial and 3D localization accuracy for any DOF. In particular, DH-PSF provides a low 3D-CRB over any desired range. DH-PSF systems can be implemented as simple modifica-

tions of traditional microscopes with the addition of a fixed mask in the back focal plane of the objective lens and only one detection plane [6]. These results are significant for localization experiments involving small particles or single molecules and should help optimize experimental parameters and imaging methodologies.

This work was supported by the National Science Foundation (NSF) award DBI-0852885.

<sup>†</sup>The current address of S. R. P. P. is KLA-Tencor, One Technology Drive, Milpitas, California 95035, USA.

## References

1. R. E. Thompson, D. R. Larson, and W. W. Webb, *Biophys. J.* **82**, 2775 (2002).
2. A. Yildiz, J. N. Forkey, S. A. McKinney, T. Ha, Y. E. Goldman, and P. R. Selvin, *Science* **300**, 2061 (2003).
3. S. K. Kufer, M. Strackharn, S. W. Stahl, H. Gump, E. M. Puchner, and H. E. Gaub, *Nat. Nanotech.* **4**, 45 (2009).
4. E. Betzig, G. H. Patterson, R. Sougrat, O. W. Lindwasser, S. Olenych, J. S. Bonifacino, M. W. Davidson, J. Lippincott-Schwartz, and H. F. Hess, *Science* **313**, 1642 (2006).
5. M. J. Rust, M. Bates, and X. Zhuang, *Nat. Meth.* **3**, 793 (2006).
6. A. Greengard, Y. Y. Schechner, and R. Piestun, *Opt. Lett.* **31**, 181 (2006).
7. S. Ram, J. Chao, P. Prabhat, E. S. Ward, and R. J. Ober, *Proc. SPIE* **6443**, 64430D (2007).
8. S. R. P. Pavani and R. Piestun, *Opt. Express* **16**, 22048 (2008).
9. M. Speidel, A. Jonáš, and E. Florin, *Opt. Lett.* **28**, 69 (2003).
10. H. P. Kao and A. S. Verkman, *Biophys. J.* **67**, 1291 (1994).
11. B. Huang, W. Wang, M. Bates, and X. Zhuang, *Science* **319**, 810 (2008).
12. S. Ram, P. Prabhat, E. S. Ward, and R. J. Ober, *Opt. Express* **17**, 6881 (2009).
13. S. R. P. Pavani, M. A. Thompson, J. S. Biteen, S. J. Lord, N. Liu, R. J. Tweig, R. Piestun, and W. E. Moerner, *Proc. Natl. Acad. Sci. USA* **106**, 2995 (2009).
14. S. R. P. Pavani, J. G. DeLuca, and R. Piestun, *Opt. Express* **17**, 19644 (2009).
15. C. v. Middendorff, A. Egner, C. Giesler, S. W. Hell, and A. Schonle, *Opt. Express* **16**, 20774 (2008).
16. G. Shtengel, J. A. Galbraith, C. G. Galbraith, J. Lippincott-Schwartz, J. M. Gillette, S. Manley, R. Sougrat, C. M. Waterman, P. Kanchanawong, M. W. Davidson, R. D. Fetter, and H. F. Hess, *Proc. Natl. Acad. Sci. USA* **106**, 3125 (2009).
17. M. J. Mlodzianoski, M. F. Juetten, G. L. Bean, and J. Bewersdorf, *Opt. Express* **17**, 8264 (2009).
18. S. R. P. Pavani and R. Piestun, *Opt. Express* **16**, 3484 (2008).
19. R. Piestun, B. Spektor, and J. Shamir, *J. Opt. Soc. Am. A* **13**, 1837 (1996).